



Contents lists available at ScienceDirect

# Journal of Magnetic Resonance

journal homepage: [www.elsevier.com/locate/jmr](http://www.elsevier.com/locate/jmr)



## Active control of the spatial MRI phase distribution with optimal control theory



Pauline M. Lefebvre <sup>a,\*<sup>1</sup></sup>, Eric Van Reeth <sup>a,1</sup>, Hélène Ratiney <sup>a</sup>, Olivier Beuf <sup>a</sup>, Elisabeth Brusseau <sup>a</sup>, Simon A. Lambert <sup>a</sup>, Steffen J. Glaser <sup>b</sup>, Dominique Sugny <sup>c,d</sup>, Denis Grenier <sup>a</sup>, Kevin Tse Ve Koon <sup>a</sup>

<sup>a</sup> Univ.Lyon, INSA-Lyon, Université Claude Bernard Lyon 1, UJM-Saint Etienne, CNRS, Inserm, CREATIS UMR 5220, U1206, 3 rue Victor Grignard, F-69616 Lyon, France

<sup>b</sup> Department of Chemistry, Technische Universität München, Lichtenbergstraße 4, D-85748 Garching, Germany

<sup>c</sup> ICB, UMR 6303 CNRS-Université de Bourgogne, 9 avenue Alain Savary, F-21078 Dijon, France

<sup>d</sup> Institute for Advanced Study, Technische Universität München, Lichtenbergstraße 2a, D-85748 Garching, Germany

### ARTICLE INFO

#### Article history:

Received 14 February 2017

Revised 11 May 2017

Accepted 15 May 2017

Available online 22 May 2017

#### Keywords:

Optimal control theory

MRI phase

RF pulses design

Phase control

MR elastography

### ABSTRACT

This paper investigates the use of Optimal Control (OC) theory to design Radio-Frequency (RF) pulses that actively control the spatial distribution of the MRI magnetization phase. The RF pulses are generated through the application of the Pontryagin Maximum Principle and optimized so that the resulting transverse magnetization reproduces various non-trivial and spatial phase patterns. Two different phase patterns are defined and the resulting optimal pulses are tested both numerically with the ODIN MRI simulator and experimentally with an agar gel phantom on a 4.7 T small-animal MR scanner. Phase images obtained in simulations and experiments are both consistent with the defined phase patterns. A practical application of phase control with OC-designed pulses is also presented, with the generation of RF pulses adapted for a Magnetic Resonance Elastography experiment. This study demonstrates the possibility to use OC-designed RF pulses to encode information in the magnetization phase and could have applications in MRI sequences using phase images.

© 2017 Elsevier Inc. All rights reserved.

## 1. Introduction

Magnetic Resonance Imaging (MRI) techniques using the phase instead or in addition to the magnitude of the MR signal are increasingly developing. Phase images provide valuable information in various MRI applications, as for example information on flow velocity [1] (phase-contrast cine MR imaging), magnetic susceptibility [2] (Susceptibility Weighted Imaging), viscoelastic properties [3] (Magnetic Resonance Elastography, MRE) or temperature [4] (MRI thermometry). Other phase-based sequences, such as Diffusion Tensor MRI (DTI) [5], use spin phase shift to modify the signal intensity and thus extract information from signal attenuation.

\* Corresponding author at: Univ. Lyon, INSA-Lyon, Université Claude Bernard Lyon 1, UJM-Saint Etienne, CNRS, Inserm, CREATIS UMR 5220, U1206, 3 rue Victor Grignard, F-69616 Lyon, France.

E-mail addresses: [pauline.lefebvre@creatis.insa-lyon.fr](mailto:pauline.lefebvre@creatis.insa-lyon.fr) (P.M. Lefebvre), [eric.van-reeth@creatis.insa-lyon.fr](mailto:eric.van-reeth@creatis.insa-lyon.fr) (E. Van Reeth), [helene.ratiney@creatis.insa-lyon.fr](mailto:helene.ratiney@creatis.insa-lyon.fr) (H. Ratiney), [olivier.beuf@creatis.insa-lyon.fr](mailto:olivier.beuf@creatis.insa-lyon.fr) (O. Beuf), [elisabeth.brusseau@creatis.insa-lyon.fr](mailto:elisabeth.brusseau@creatis.insa-lyon.fr) (E. Brusseau), [simon.lambert@creatis.insa-lyon.fr](mailto:simon.lambert@creatis.insa-lyon.fr) (S.A. Lambert), [steffen.glaeser@tum.de](mailto:steffen.glaeser@tum.de) (S.J. Glaser), [dominique.sugny@u-bourgogne.fr](mailto:dominique.sugny@u-bourgogne.fr) (D. Sugny), [denis.grenier@creatis.insa-lyon.fr](mailto:denis.grenier@creatis.insa-lyon.fr) (D. Grenier), [kevin.tsevekoon@creatis.insa-lyon.fr](mailto:kevin.tsevekoon@creatis.insa-lyon.fr) (K. Tse Ve Koon).

<sup>1</sup> These authors have contributed equally.

In these phase-based MRI techniques, the phase-encoding process is mainly handled with gradients, which often present physical limitations such as maximum amplitude or switching rate. For example, strong gradients are typically used in DTI sequences, and their switching induce eddy currents [5]. This can cause geometrical distortions and therefore lead to significant errors in the estimation of diffusion parameters. In MRE, motion-encoding gradients typically oscillate at the same frequency as the harmonic motion induced in the tissue. However gradient commutations are physically limited by the slew rate of the gradient system and therefore high frequencies are not achievable: standard clinical systems can hardly encode wave motion for frequencies higher than 1 kHz.

The objective of this paper is to present a novel approach, exclusively based on RF pulses designed with Optimal Control (OC) theory in combination with a constant gradient, to encode the phase information. Magnetization phase is actively controlled, spatially and temporally, during the application of the RF pulse. The main benefit of this approach lies in the fact that the phase information is encoded during the excitation process: the signal can be immediately acquired after the application of the RF pulse, with extremely short TE values. By comparison, classical approaches for

phase-encoding use post-excitation gradients, and thus suffer from  $T_2$  or  $T_2^*$  signal decay before acquisition.

Phase control with RF pulses has been investigated in some studies on selective pulse design. Shinar Le Roux (SLR) pulses [6,7] can generate for example a quadratic phase pattern with the design of a FIR filter. Carlson [8,9] used Inverse Scattering Theory (IST) to design selective excitation pulses and control the phase distribution. The latter work aimed at finding a method to design pulses that give a flat phase distribution and that remove non-linear phase contributions. Both semi-analytical solutions (SLR and IST) are no longer applicable when there is a dynamic perturbation of the magnetic field, as in MRE. Moreover, these pulse design methods cannot fully control the phase distribution in the Bloch sphere.

The use of OC for RF pulse design in MRI has already been performed in different contexts [10]: we can mention studies on robust (regarding field inhomogeneities) excitation and refocusing [11–14], contrast optimization [15–18] or parallel transmit [19–21]. The possibility to control the phase with OC has been mentioned and investigated in NMR studies [22,23] and has been applied to create delayed echo sequences in MRI [24]. However, the use of OC pulses to create a controlled macroscopic spatial phase distribution for imaging applications has never been explored. As a proof-of-concept, in this paper, RF pulses are designed to achieve different non-trivial and spatial phase patterns, represented as different target-states in the transverse plane of the Bloch sphere (Section 3). These RF pulses are, in a second step, integrated into classical MRI sequences: simulations with the Object Oriented Development Interface for NMR (ODIN) [25] (Section 4) and experiments on a small-animal MRI scanner (Section 5) with an agar phantom are performed.

An application of phase control with OC pulses is also presented in this article, to illustrate a practical application of RF-based phase control. An MRE experiment is performed, in which the wave propagation is directly encoded in the phase image with the optimal RF pulse and a constant gradient. Unlike the classical approach, no post-excitation Motion-Encoding Gradients (MEG) are required.

A method for motion detection without oscillating MEG, has already been proposed in a previous paper [26]. This method is principally based on a hardware development, with a RF field gradient obtained from a ladder-shape coil, and can detect a mechanical vibration (and its direction, frequency and amplitude) but does not give a 2D phase image showing wave propagation. Our approach (optimal RF and constant gradient) aims at yielding results similar to those obtained from standard encoding scheme with oscillating gradients.

## 2. Method: optimal control theory

### 2.1. Optimal control theory framework in MRI

Optimal control theory, with the application of the Pontryagin Maximum Principle (PMP) [27], enables the computation of the optimal trajectory of a dynamic system – with regards to a given optimality criterion – and its associated control.

In MRI application, the dynamic system corresponds to the macroscopic magnetization  $\vec{M} = (M_x, M_y, M_z)$  of spin ischromats (defined in the Bloch sphere), whose evolution is governed by the Bloch equation:

$$\frac{d}{dt} \begin{pmatrix} M_x \\ M_y \\ M_z \end{pmatrix} = \begin{pmatrix} -\frac{1}{T_2} & \Delta_{B_0} & -\omega_y \\ -\Delta_{B_0} & -\frac{1}{T_2} & \omega_x \\ \omega_y & -\omega_x & -\frac{1}{T_1} \end{pmatrix} \begin{pmatrix} M_x \\ M_y \\ M_z \end{pmatrix} + \begin{pmatrix} 0 \\ 0 \\ \frac{M_0}{T_1} \end{pmatrix} \quad (1)$$

with  $\Delta_{B_0}$  being the resonance offset,  $T_1$  and  $T_2$  the longitudinal and transverse relaxation times,  $\vec{\omega} = (\omega_x, \omega_y)$  the  $x$  and  $y$  components of the RF pulse (corresponding to the control field of this optimal control problem) that will bring the macroscopic magnetization to the user-defined target-state.

### 2.2. Pontryagin Maximum Principle

The OC problem is solved here with the application of the Pontryagin Maximum Principle [27]. The PMP is formulated from the definition of a pseudo-Hamiltonian:

$$H = \vec{P} \cdot \dot{\vec{M}} \quad (2)$$

where  $\vec{P}$  is the costate vector. It can be interpreted in this optimization problem as a Lagrange multiplier associated to  $\vec{M}$ .

The PMP states that the optimal control  $\vec{\omega}^{opt}$  must maximize the Hamiltonian during the control time. Then, the optimal trajectories ( $\vec{M}^{opt}$  and  $\vec{P}^{opt}$ ) satisfy the following Hamiltonian equations:

$$\dot{\vec{M}}^{opt} = \frac{\partial H}{\partial \vec{P}^{opt}} \quad \text{and} \quad \dot{\vec{P}}^{opt} = -\frac{\partial H}{\partial \vec{M}^{opt}} \quad (3)$$

Moreover, the optimal trajectories must satisfy the following boundaries conditions:

$$\vec{M}^{opt}(t_0) = \begin{pmatrix} 0 \\ 0 \\ M_0 \end{pmatrix} \quad \text{and} \quad \vec{P}^{opt}(t_f) = -\frac{\partial C}{\partial \vec{M}^{opt}(t_f)} \quad (4)$$

with  $C$  being the cost function defined by the user to achieve the desired target-state,  $t_0$  and  $t_f$  respectively the initial and final time of the control duration. Initial magnetization  $\vec{M}(t_0)$  is chosen here at the equilibrium state.

### 2.3. GRAPE algorithm

This optimal control problem is solved with a purely numerical approach using the GRAPE (GRAdient Ascent Pulse Engineering) algorithm [28], which is a gradient ascent algorithm introduced for Nuclear Magnetic Resonance pulse design. It was implemented for this study on Matlab (The MathWorks, R2014b).

#### 2.3.1. Steps of the algorithm

This part presents the different steps of the GRAPE algorithm as initially proposed. Starting from an initial control field (defined by the user), this algorithm iteratively minimizes the cost function by adjusting the control field at each iteration, while fulfilling the PMP constraints. The different steps are:

1. Choice of the initial control field  $\vec{\omega}^0$ .
2. Forward propagation of  $\vec{M}$ , from  $t = t_0$  to  $t_f$ , starting from  $\vec{M}_0$  (defined from initial boundary condition (4)).
3. Backward propagation of  $\vec{P}$ , from  $t = t_f$  to  $t_0$ , starting from  $\vec{P}_{t_f}$  (defined from final boundary condition (4) and  $\vec{M}_{t_f}$ ).
4. Update of the control field: computation of the following control field  $\vec{\omega}^{(k+1)}$  from control field  $\vec{\omega}^{(k)}$  with:

$$\vec{\omega}^{(k+1)} = \vec{\omega}^{(k)} - \alpha \frac{\partial C}{\partial \vec{\omega}} \quad (5)$$

with  $\alpha > 0$  the convergence step.

5. Repetition of steps 2–4 until the convergence criterion is reached.

The gradient term  $\frac{\partial C}{\partial \vec{\omega}}$  can be expressed as a function of the backward propagation of the costate vector and forward propagation of the magnetization vector and depends therefore only on two full time evolutions.

### 2.3.2. Algorithm implementation details

The cost function gradient  $\frac{\partial C}{\partial \vec{\omega}}$  needs to be calculated with an accurate approximation in order to ensure fast and correct convergence. We use here complex differentiation [29,30] to estimate this cost function derivative. Let  $f$  be a real function of  $h$  defined on real space, a small imaginary increment  $i\varepsilon$  is added to  $h$  and the Taylor series of  $f(h)$  writes:

$$f(h + i\varepsilon) = f(h) + i\varepsilon f'(h) - \frac{\varepsilon^2}{2} f''(h) + \dots \quad (6)$$

Assuming that  $\varepsilon$  is small enough ( $\varepsilon \ll 1$ ),  $f'(h)$  can be expressed as:

$$f'(h) \approx \frac{\text{Im}(f(h + i\varepsilon))}{\varepsilon} \quad (7)$$

The use of Eq. (7) as a derivative approximation significantly improves the estimation accuracy compared to finite differences, which is affected by subtractive cancelation when small values of  $\varepsilon$  are used. In the following sections,  $\varepsilon$  is set to  $10^{-10}$ .

In the initial version of GRAPE algorithm [28], update of the control field (step 4) is performed iteratively with a constant convergence step  $\alpha$ . In this study, in order to improve the convergence speed and accuracy (compared to the simple gradient ascent optimization method used in Eq. (5)), a second order approximation scheme was performed, with the implementation of a LBFGS quasi-Newton algorithm detailed in [31].

## 3. RF pulse generation with OC for phase control

### 3.1. Definition of cost function

Optimal control framework requires the formulation of a cost function, that will be minimized during the optimization process.

The purpose of this paper is to control the magnetization phase, and therefore to bring the magnetization of spins in a defined target-state in the transverse plane  $\vec{M}_{TS}^\perp = (M_X, M_Y)$  of the Bloch sphere. We define the cost function to be minimized as:

$$C(\omega_x, \omega_y) = \sum_i \|\vec{M}_i^\perp(t_f) - \vec{M}_{i,TS}^\perp\|^2 \quad (8)$$

This cost function computes the quadratic error between two magnetization distributions, one being the target-state  $\vec{M}_{i,TS}^\perp$  (defined in more details in the next part) and the other one being the state of magnetization at the end of the RF pulse  $\vec{\omega}$ . Depending on the spin position (index  $i$ ), spins magnetization  $\vec{M}_i^\perp(t_f)$  will be assigned a specific target-state  $\vec{M}_{i,TS}^\perp$ .

### 3.2. Definition of target-states and phase patterns

First, the target-states defined below are in the transverse plane  $(M_X, M_Y)$  of the Bloch sphere. Therefore, this implies that  $|\vec{M}^\perp| = 1$  which leads to a resulting flip angle equal to  $\pi/2$ .

Then, for each spin isochromat, the target-state will depend on their position  $i$  in a given direction, here chosen to be the readout.

Spin isochromats positions are discriminated through the application of a gradient, which will be called the *phase sensitizing gradient* and noted  $G_{OC}$ , applied in the readout direction during the optimal RF pulse. Thus, the pulse will lead isochromats to a certain state in the transverse plane, depending on their resonance frequency offset  $f_i$ .

The frequency resonance offset range  $\Delta f$  (proportional to the magnetic field offset) that should be controlled for a field of view  $FOV_x$  in the readout direction (let us denote  $x$  this direction) is:

$$\Delta f = \frac{\gamma}{2\pi} \cdot G_{OC} \cdot FOV_x. \quad (9)$$

This controlled resonance offset range, set to 10 kHz for all calculated pulses, is discretized in 200 equidistant parts for the resolution of the numerical optimal control problem: it results in a frequency resolution of  $d\Delta f = 50$  Hz. Moreover, this resonance offset range is divided in three or four (depending on the defined phase pattern) intervals, to which are assigned a different target-state in the transverse plane.

Two different non-trivial phase patterns in the transverse plane  $(M_X, M_Y)$  of the Bloch sphere were defined in this study, corresponding to different phase image patterns.

Pattern A presents four different areas, with different constant values of phase: 0,  $\pi$ , 0 and  $\pi$ . Pattern B consists in having three different phase evolutions along the readout direction: a linear phase increase from 0 to  $\pi$ , a constant level equal to  $\pi$  and a linear decrease from  $\pi$  to 0. They are represented in Fig. 1, with their corresponding profiles along the readout direction.

### 3.3. RF pulses generation for phase image control

#### 3.3.1. Initialization and temporal resolution of the RF pulses

The initial control field  $\vec{\omega}^0(t)$  for both generations of RF pulses was set to a constant value:  $|\vec{\omega}^0(t)| = 50$  Hz and a phase equal to 0.

As the optimal control problem gives here a numerical solution of the optimal RF pulses, they should be discretized in  $N$  time steps of duration  $\Delta t$  during the time interval  $[t_0, t_f]$ . In this work, the following values were chosen:  $N = 300$ ,  $t_f = 6$  ms and consequently,  $\Delta t = 20$   $\mu$ s.

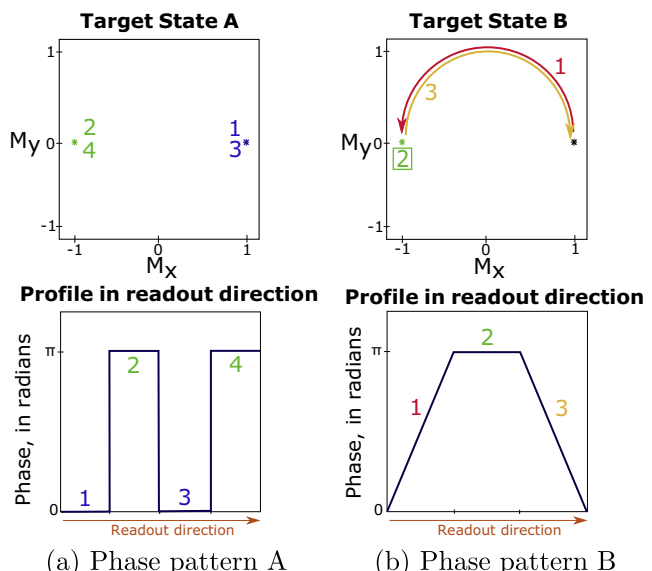


**Fig. 1.** Illustration of the two phase patterns defined for the phase control experiment with optimal control theory. Top row represents the spin target positions in the transverse plane  $(M_X, M_Y)$  of the Bloch sphere. Bottom row displays the profile of spin isochromats phases along the readout direction.

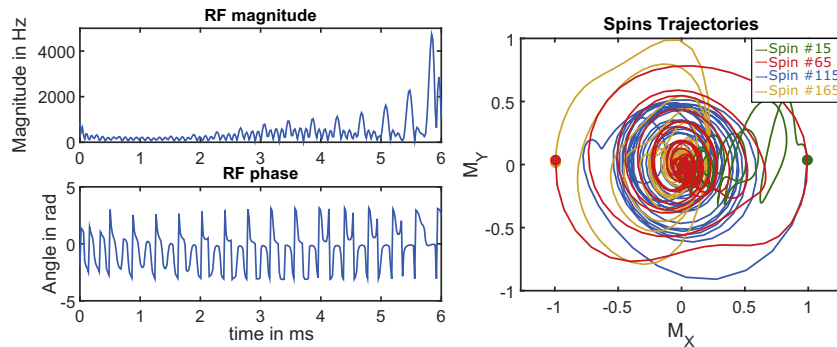


**Fig. 2.** Magnitude and phase of the optimal RF pulse associated to phase pattern A as a function of time. Projections in the transverse plane of the trajectories of selected spin isochromats belonging to the different frequency intervals are displayed on the right: Spin 15 (resp. 65, 115 and 165) corresponds to a resonance offset belonging to the first (resp. second, third and fourth) area of the pattern displayed on Fig. 1(a). Final states are marked with a dot.

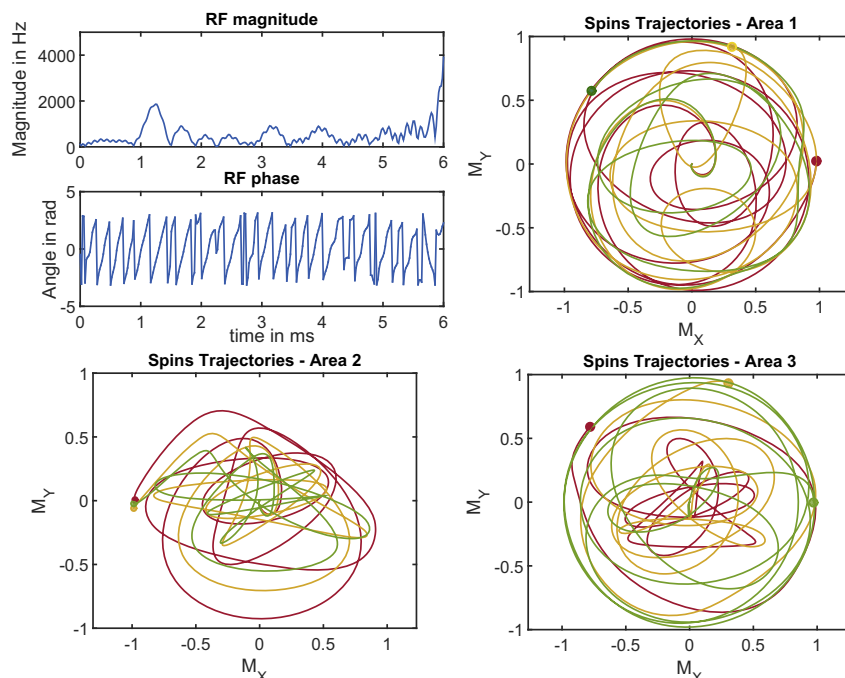


**Fig. 3.** Magnitude and phase of the optimal RF pulse associated to phase pattern B as a function of time. Projections of the spin isochromat trajectories in the transverse plane of the Bloch sphere are displayed on different figures for each target-state area (see on Fig. 1(b)): three different resonance offsets were taken in each of the three areas of the pattern. Final states are marked with a dot.

### 3.3.2. Relaxation times

RF pulses were generated with  $T_1$  and  $T_2$  values corresponding to the ones of the agar gel phantom (agar concentration 1.5% in weight) used in the MRI experiments, i.e.  $T_1 = 1500$  ms and  $T_2 = 130$  ms.

### 3.3.3. Optimal RF pulses

Figs. 2 and 3 present the two computed RF pulses A and B (magnitude and phase as a function of time). These figures also show the simulated magnetization trajectories of spin isochromats, projected in the transverse plane. The different trajectories correspond to the temporal evolution of isochromats with different target-states, during the application of computed pulses.

For the pulse A, the trajectories of the 15<sup>th</sup>, 65<sup>th</sup>, 115<sup>th</sup> and 165<sup>th</sup> spin isochromats whose resonance offset frequencies are in the range  $\Delta f = 200 \times d\Delta f$  (belonging respectively to area 1, 2, 3 and 4) are plotted. For clarity purpose, the spin isochromats trajectories of pulse B are divided in three plots, corresponding to the three defined areas (linear increase, constant level and linear decrease of the phase).

and 4) are plotted. For clarity purpose, the spin isochromats trajectories of pulse B are divided in three plots, corresponding to the three defined areas (linear increase, constant level and linear decrease of the phase).

Final states are marked with a dot: these spins isochromats trajectories plots highlight the good convergence of the OC pulses, as final states are very close to the target-states defined on Fig. 1.

Finally, for the RF pulse corresponding to phase pattern B, the resulting phase for different resonance offsets (blue<sup>2</sup> asterisks) is presented on Fig. 4 and compared to the profile of the target phase (dark line). This figure also highlights the correct convergence of the algorithm for pulse B: the resulting magnetization phase associated with pulse B is very close to the profile of the target phase pattern.

<sup>2</sup> For interpretation of color in Fig. 4, the reader is referred to the web version of this article.

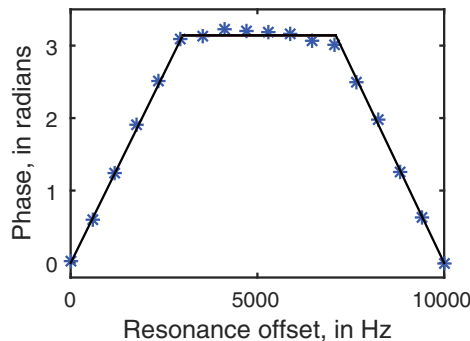


**Fig. 4.** Phase profile as a function of resonance offset (as a reminder, frequency resonance offset range is set to 10 kHz for all pulses), obtained from pulse B (blue asterisks), and compared to the profile of the target phase pattern (dark line). (For interpretation of the references to color in this figure legend, the reader is referred to the web version of this article.)

#### 4. MRI simulations of phase control with ODIN

##### 4.1. Simulation conditions

Simulations were performed using the MRI simulator ODIN [25]. ODIN is a C++ software framework designed to develop and simulate MR sequences. Once a virtual phantom and an MRI sequence have been specified, it propagates the Bloch equations in the defined virtual phantom throughout the whole sequence.

##### 4.1.1. Generation of virtual phantom

A virtual phantom is generated by specifying the values of  $T_1$ ,  $T_2$  and proton density. For this work, a homogeneous phantom was defined by using the  $T_1$  and  $T_2$  values of the agar phantom used in our experiments and the phantom dimensions were set to  $20 \times 20 \times 3$  mm.

##### 4.1.2. Sequence parameters

A spin-echo sequence, adapted for the OC pulse experiment, was implemented in ODIN. To discriminate spin isochromats positions along the readout direction, the phase sensitizing gradient  $G_{OC}$  was applied simultaneously with the OC pulse. The slice selective gradient, applied usually during the excitation pulse, was removed, but the refocusing pulse was kept selective. A chronogram of the sequence is presented on Fig. 5.

The echo-time was set to the minimum value possible in order to limit signal loss and dephasing, and was fixed to  $TE = 6.6$  ms. In this OC-based acquisition, the echo-time is defined as the time between the end of the RF pulse and the middle of the acquisition (peak of signal). The repetition-time was sufficiently long to ensure full longitudinal magnetization relaxation, and was fixed to  $TR = 5$  s. The phase sensitizing gradient  $G_{OC}$  was fixed to  $11.7$  mT/m,

according to Eq. (9) with frequency range  $\Delta f = 10$  kHz and  $FOV_x = 20$  mm. Bandwidth of the acquisition was equal to 25 kHz. Matrix size was  $64 \times 64$  pixels.

#### 4.2. Results

Magnitude and phase images resulting from ODIN simulations are presented on Fig. 6, for both optimal RF pulses A and B. Moreover, the mean phase value for each column of the phase images has been calculated and the resulting profiles plotted.

For both pulses, phase and magnitude images are consistent with the expected results. The slight phase decrease in area 2 of pulse B is consistent with the simulated profile obtained from pulse B, as shown on Fig. 4. Standard deviations of the magnitude images were calculated over the whole phantom and normalized by the mean value, excluding phase transitions areas, and are presented in Table 1: signal magnitude presents very small standard deviations for the two cases and is therefore nearly constant, as expected.

In order to quantify the magnitude variation in the phase transition areas, the maximum variation on magnitude images was also calculated with the following formula:

$$Max_{var} = \frac{\bar{I} - Min_l}{\bar{I}},$$

with  $\bar{I}$  the mean value on the magnitude image and  $Min_l$  the minimum magnitude value. Maximum variation is quite high for magnitude image resulting from pulse A. This magnitude image presents actually an area with very low magnitude, corresponding to the transition  $\pi \rightarrow 0$ .

For each area of phase images (except areas 1 and 3 of pulse B), a Region of Interest was defined by taking all pixels within the considered area, and mean and standard deviation were extracted. Results are presented in Table 1. Phase values in the different areas correspond to the expected ones.

For the linear phase variations of pulse B (area 1 and 3), the mean value of each column has been calculated and the obtained profile has been linearly fitted to a linear curve. The slope value normalized to the frequency offset control range (10 kHz divided in three intervals) has been extracted, with their coefficient of determination,  $R^2$ . The high values obtained for  $R^2$  (values close to 1) indicate that phase variations are linear in these two areas and the slope in both areas are close to the expected ones (expected slopes:  $\pm \frac{\pi}{10^3}$  rad/kHz =  $\pm 0.942$  rad/kHz).

Finally, the phase image from pulse A presents sharp transitions between the different areas. This demonstrates that optimal RF pulses accurately control the phase, with good frequency selectivity.

#### 5. MRI experiments on phase control

##### 5.1. Experimental conditions

Experiments were carried out on a homogeneous agar phantom (agar concentration 1.5% in weight).  $T_1$  and  $T_2$  values were measured using an exponential fit of the water peak acquired with a localized Point RESolved Spectroscopy (PRESS) sequence, for different TE and TR. They were found to be  $T_1 = 1500$  ms and  $T_2 = 130$  ms. The phantom was cylindrically-shaped, with a diameter equal to 27 mm and a height of 50 mm.

MRI measurements were run on a Bruker 4.7 T small-animal MRI system, with a cylindrical inner-diameter 30 mm bird-cage mouse coil. A spin-echo sequence, similar to the one used for ODIN simulations (Fig. 5), was used with  $64 \times 64$  matrix and  $FOV = 3.25 \times 3.25$  cm $^2$ .  $G_{OC}$  was set to 8 mT/m, according to Eq.

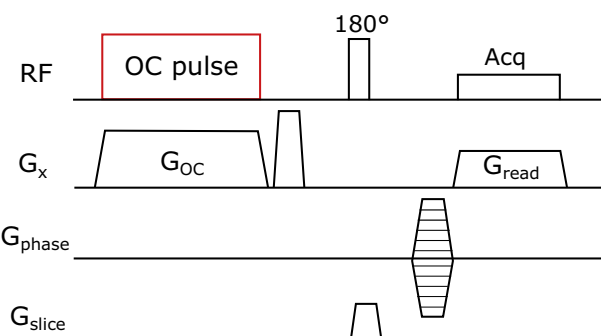


**Fig. 5.** ODIN spin-echo sequence adapted for the optimal control pulse experiment.

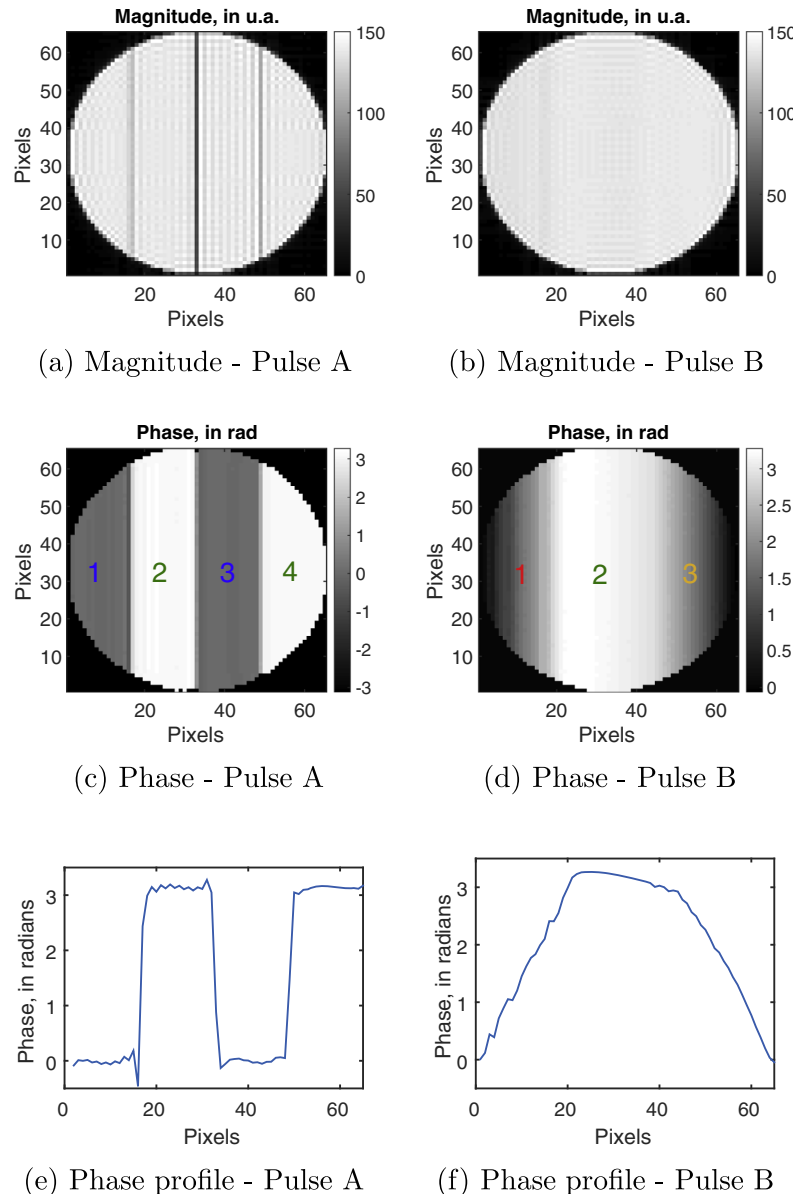


**Fig. 6.** Magnitude and phase (in radians) images obtained from ODIN MRI simulations, with the two RF pulses A and B (FOV = 4 × 4 cm<sup>2</sup> and matrix = 64 × 64 pixels) and corresponding mean phase profiles on bottom row.

**Table 1**

Standard deviations (std) and maximum variations ( $Max_{var}$ ) of magnitude images. Mean values of phase (with corresponding standard deviations) of the different areas of phase images, in radians, and slopes for linear variations, obtained from the two different pulses A and B (Figs. 6 and 7).

			ODIN	MRI
Pulse A	Area	Expected phase		
	1	0	-0.01 ± 0.14	-0.16 ± 0.17
	2	$\pi$	3.13 ± 0.06	2.99 ± 0.07
	3	0	-0.01 ± 0.18	-0.20 ± 0.08
	4	$\pi$	3.12 ± 0.13	3.02 ± 0.07
	Standard deviation of magnitude		4.0%	8.6%
	$Max_{var}$		0.62	0.70
Pulse B	Area	Expected phase or slope		
	1	0.942 rad/kHz	0.950 ( $R^2 = 0.986$ )	0.969 ( $R^2 = 0.995$ )
	2	$\pi$	3.12 ± 0.11	3.02 ± 0.09
	3	-0.942 rad/kHz	-0.893 ( $R^2 = 0.999$ )	-0.888 ( $R^2 = 0.996$ )
	Standard deviation of magnitude		3.1%	7.3%
	$Max_{var}$		0.04	0.07

(9). Optimal RF pulses used in the following two MRI experiments were exactly the same as the ones used for the ODIN simulations. The echo-time was set to 9.8 ms and the repetition-time to 5 s.

### 5.2. Slice selectivity

The optimal RF pulses are applied without slice selective gradients. Therefore the obtained signal comes from the overall sample. In order to get rid of refocused artefactual signal coming from extremities of the phantom, spatial saturation bands were added in the slice direction and, similarly to the Odin simulation, the refocusing pulse was kept selective.

### 5.3. Results

**Fig. 7** presents the resulting magnitude and phase images obtained from MRI measurements, for both optimal pulses A and B. The mean phase of each column on the phase images has been calculated and the resulting profiles are also presented on **Fig. 7**.

Here again, magnitude and phase images are consistent with expected results. Acquired magnitude images are nearly homogeneous in the whole phantom, as shown on **Table 1**, except for regions close to the coil, corresponding to the B1 magnetic field inhomogeneities coming from the copper rungs of the volume coil. Phase values, presented in **Table 1**, also correspond well to the defined target-states. A slight difference of less than 0.2 rad s<sup>-1</sup> can be observed between expected values and obtained phase patterns.

Finally, resulting phase image from pulse A presents the same sharp profiles than the ones obtained in simulation, showing that the RF pulses accurately control the phase in real conditions.

### 6. An example of application: Magnetic Resonance Elastography

Results presented in previous parts validate the possibility to accurately control the magnetization phase with RF pulses, in a simple experiment with a static resonance offset applied (through a gradient) during the pulse. A practical application of this phase control

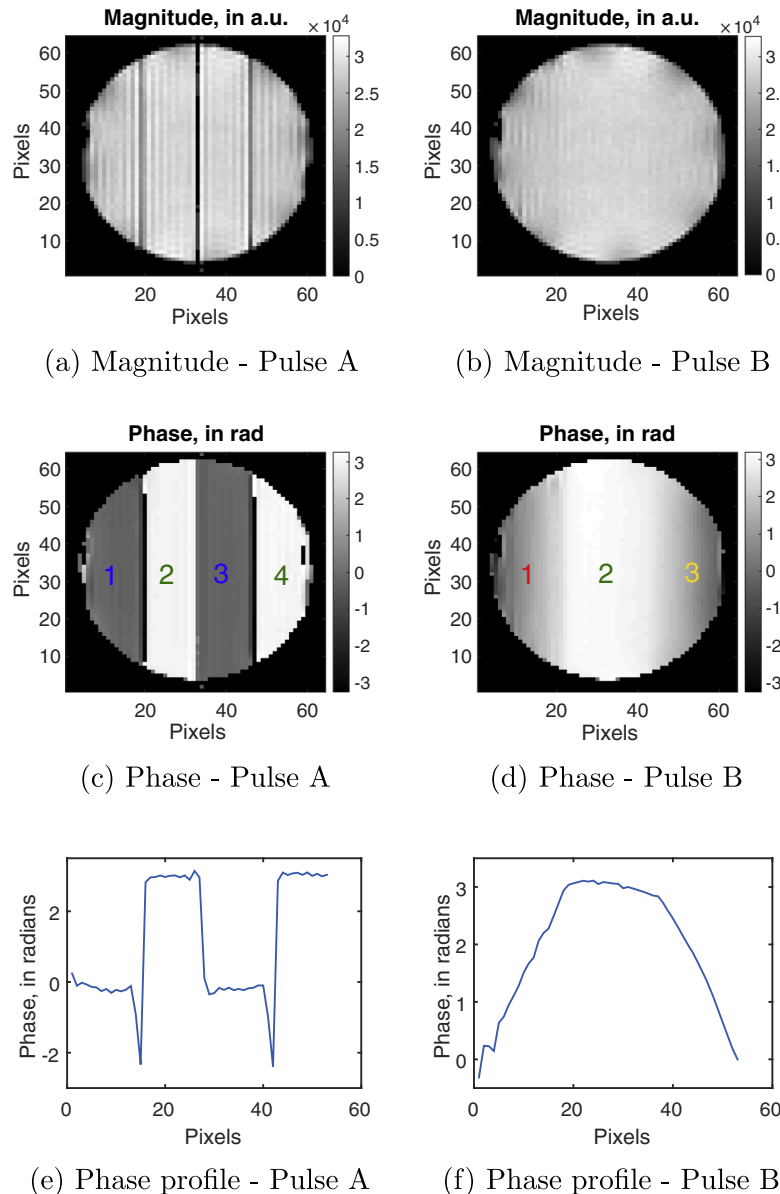


**Fig. 7.** Magnitude and phase (in radians) images obtained from MRI measurements, with the two optimal RF pulses A and B (FOV = 4 × 4 cm<sup>2</sup> and matrix = 64 × 64 pixels), and corresponding mean phase profiles on bottom row.

is now presented with the generation of RF pulses adapted for Magnetic Resonance Elastography. This is a more complex framework as, in this application, the resonance offset  $\Delta B_0$  is time-dependant and thus changes during the application of the RF pulse.

What is proposed here is to use a constant gradient, applied in the motion direction during the RF pulse, with no further encoding. Spins position along the wavelength will be discriminated depending on the magnetic field variation coming from the wave propagation coupled with the constant gradient, and the RF pulse will then lead spins in different final positions. The aim is to obtain at the end of the RF pulse a linear magnetization phase distribution that encodes the wave propagation.

### 6.1. Introduction on Magnetic Resonance Elastography

Magnetic Resonance Elastography is a MR non-invasive method enabling the characterization of viscoelastic properties of tissues [3]. Shear waves are induced in the tissue of interest using an external driver. Tissue motion is then encoded in phase images with a motion-sensitive MR imaging sequence and these images are finally processed to map and quantify the viscoelastic properties of the tissue.

In MRE sequences, a periodic gradient called Motion-Encoding Gradient (MEG) is applied synchronously with the external harmonic excitation, typically at the same frequency and along the direction of the cyclic motion of spins. The cyclic spin motion in combination with the MEG causes a measurable phase-shift in the NMR signal, proportional to the scalar product of the displacement vector and the MEG vector, and to the duration of the MEG. Acquired phase images correspond to a snapshot of the mechanical wave propagation within the tissue.

More precisely, the combination of the MEG and the motion induced by shear waves produces a change in the magnetic field perceived by spins. Assuming no delay between the MEG and the mechanical excitation, this time-dependent variation writes:

$$\Delta B_0(x, z, t) = G_z \sin(2\pi f_e t) \left( z + A \times \sin(-2\pi f_e t + 2\pi \frac{x}{\lambda}) \right) \quad (10)$$

with  $z$  the cyclic spin motion direction,  $x$  the direction of wave propagation,  $G_z$  the amplitude of the MEG in spin motion direction,  $A$  the amplitude of periodic motion,  $f_e$  the motion frequency, and  $\lambda$  the wavelength.

Phase accumulation over one period oscillation is then given by:

$$\phi(x, z) = \gamma \int_0^{1/f_e} \Delta B_0(x, z, t) dt = -\frac{\gamma G_z A}{2f_e} \cos(2\pi \frac{x}{\lambda}) \quad (11)$$

### 6.2. Adaptation of Bloch equations for MRE

**Fig. 8(a)** presents the wave propagation and coordinate system used here for the definition of the optimal control problem.

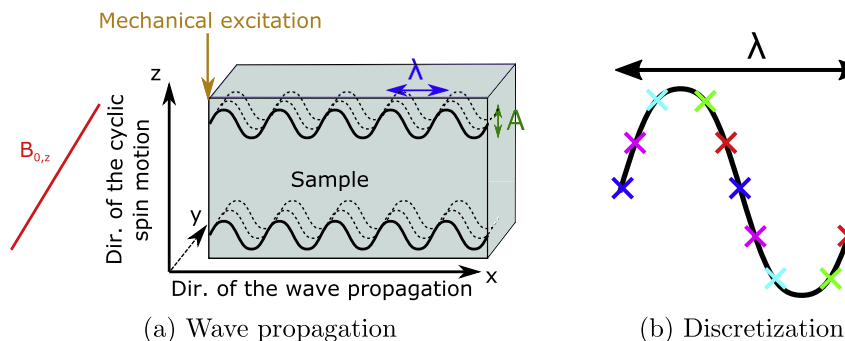


**Fig. 8.** (a) Wave propagation pattern at a fixed time. The wave propagates in the  $x$ -direction and spin motion is in the  $z$ -direction. A gradient,  $G_z$ , is applied in the  $z$ -direction. The wave oscillates at frequency  $f_e$ , corresponding to the wavelength  $\lambda$ . (b) Discretization of one wavelength into 10 phase offsets.

In this OC problem, a constant gradient is applied during the wave propagation (and the application of the RF pulse) in motion direction. Therefore, the Eq. (10) becomes:

$$\Delta B_0(x, z, t) = G_z(z + A \times \sin(-2\pi f_e t + 2\pi \frac{x}{\lambda})) \quad (12)$$

with  $G_z$  being the amplitude of the constant gradient applied in the spin cyclic motion direction. This dynamic resulting resonance offset  $\Delta B_0(t)$  is integrated in the Bloch equations (Eq. (1)) during the optimization process.

### 6.3. Definition of target-state and cost function

We propose to design a RF pulse that encodes the wave propagation in the phase image. For that purpose, we define a cost function that: (i) linearly distributes the spins phase on the interval  $[0, 2\pi]$ , and (ii) maximizes the spins transverse magnetization. The target-states thus lie on the unit circle of the normalized transverse magnetization plane. Let  $N_{spins}$  be the number of considered spins equally spaced along a wavelength of the propagation wave (**Fig. 8(b)**), and  $s \in [0, N_{spins} - 1]$  the spin index, the cost function writes:

$$C(\omega_x, \omega_y) = \sum_{s=0}^{N_{spins}-1} \left\| \vec{M}_s^\perp(t_f) - \vec{M}_{s,TS}^\perp \right\|^2 \quad (13)$$

with  $\vec{M}_{s,TS}^\perp$  the target-state vector (in the transverse plane), defined as:

$$\vec{M}_{s,TS}^\perp = \begin{pmatrix} \cos(s \times \frac{2\pi}{N_{spins}}) \\ \sin(s \times \frac{2\pi}{N_{spins}}) \end{pmatrix} \quad (14)$$

Depending on their positions along the wavelength, spins will be assigned a different magnetization phase target-state.

### 6.4. RF pulse generation

#### 6.4.1. RF pulse parameters

The RF pulse was optimized for a motion amplitude  $A = 15 \mu\text{m}$ , and for an excitation frequency  $f_e = 500 \text{ Hz}$ . A constant gradient in the spin motion direction was set to  $84 \text{ mT/m}$ . The pulse was optimized by discretizing the wavelength in  $N_{spins} = 10$  spins. Its duration was fixed to 20 ms.

#### 6.4.2. Pulse bandwidth

The constant gradient applied in the spin motion direction is also used as the slice selective gradient. The optimal pulse must ensure a consistent spins distribution throughout the whole bandwidth corresponding to the desired slice thickness. In practice, this is done by discretizing a frequency interval, on which the pulse is

optimized, and by increasing iteratively the frequency interval (and thus increasing the total number of spins to be controlled), and therefore the slice thickness until the required value is reached. The slice thickness is directly determined by the considered frequency range (bandwidth), and the strength of the gradient applied in slice direction.

In this RF pulse generation, the final frequency interval was set to 1782.5 Hz (corresponding to a slice thickness of 500  $\mu\text{m}$  with a gradient equal to 84 mT/m). The pulse was optimized throughout the frequency interval of 1782.5 Hz, with 113 steps and a frequency step equal to 15.7 Hz. Total number of controlled spins is therefore 1130 (10 spins over the wavelength are controlled).

#### 6.4.3. MRI coil physical constraints

RF pulses calculated through OC theory must respect practical constraints of the coils and the RF amplifiers used in experiments, in particular their peak amplitude. Thus, during the optimization process, the maximum RF amplitude was constrained to 2120 Hz.

[Fig. 9](#) presents the generated RF pulse (magnitude and phase).

#### 6.5. Simulation with ODIN

A dynamic numerical phantom, with dimensions  $4 \times 4 \text{ cm}^2$ , was generated with pre-defined  $T_1$  and  $T_2$  maps (same as for MRI experiments, see below). Two different motion wavelengths were simulated in two different numerical phantoms. The effect of the motion in the virtual phantom was directly encoded as a  $B_0$  field shift [\[32\]](#), given by:

$$\Delta B_0(x, t) = AG_z \times \sin\left(-2\pi f_e t + 2\pi \frac{\lambda}{\lambda}\right) \times e^{-\alpha x} \quad (15)$$

with  $G_z$  set to 84 mT/m,  $\lambda$  the wavelength of the propagating wave set to 10 mm in the first simulation and to 15 mm in the second simulation. The exponential term  $\alpha$  represents the attenuation of the wave during its propagation, due to viscosity effects, and was fixed to  $50 \text{ m}^{-1}$ . A gradient-echo sequence was used: the echo-time was set to 4 ms and the repetition-time to 1500 ms.

Resulting phase images, with the optimal RF pulse (plotted on [Fig. 9](#)), are presented on [Fig. 10](#) for the two different numerical phantoms (with  $\lambda = 10 \text{ mm}$  and  $\lambda = 15 \text{ mm}$ ) with their profiles along the propagation direction. Phase profiles are consistent with expected linear phase distributions, from  $-\pi$  to  $\pi$ , over one wavelength. Both phase profiles have a wavelength that corresponds to the value attributed to the phantom during phantom generation (10 mm and 15 mm). As a reminder, both simulations have been

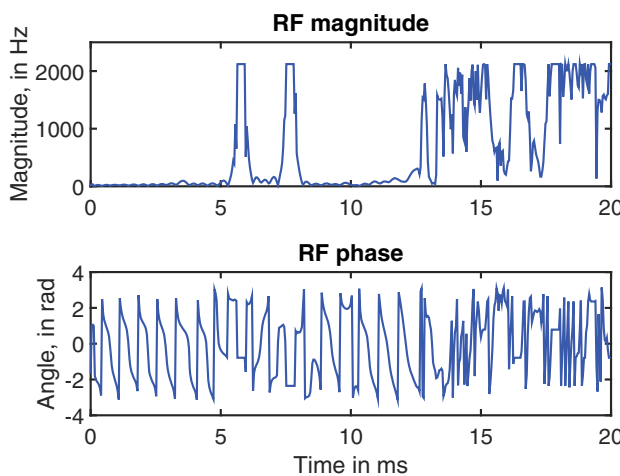


[Fig. 9](#). Magnitude and phase of the optimal RF pulse associated to the elastography problem, as a function of time.

carried out with the same constant gradient  $G_z$ . Note that the phase profiles are not affected by the wave attenuation, as expected.

#### 6.6. MRE experiment

##### 6.6.1. Acquisition of phase images

The MRE experiments were performed on a Bruker 4.7 T MRI system, with a 70 mm volume coil. Shear waves were induced in the phantom using a non-invasive custom-made device maintaining the medium between two plates [\[33\]](#), the upper one being fixed while the lower one being activated by a piezoelectric actuator (CEDRAT Technologies). Acquisitions were performed for an excitation frequency equal to 500 Hz, corresponding to the one used for the pulse generation.

A standard plastisol phantom was prepared (*Plastileurre Standard*, Bricoleurre, France), as its response to an excitation frequency of 500 Hz was already characterized [\[33\]](#).  $T_1$  and  $T_2$  values were found to be 300 and 25 ms respectively with a PRESS sequence.

The MR sequence was a gradient-echo sequence, with an echo-time equal to 1.9 ms, a repetition-time set to 1500 ms, a  $\text{FOV} = 4 \times 4 \text{ cm}^2$ ,  $64 \times 64$  matrix, and 2 accumulations.

Similarly to usual MRE experiments [\[34\]](#), the acquisition was performed twice, with a  $180^\circ$  phase shift of the wave propagation in the second acquisition, and phase-difference images have been calculated in order to remove static phase contributions. For both cases, data for four different phase offsets (equidistant over one cycle) have been acquired, giving four different snapshots of the wave propagation through the phantom.

Resulting phase-difference images, at two different phase offsets of the wave propagation, are displayed in [Fig. 11](#). No filtering was applied to these phase images. Despite the presence of noise, wave pattern is clearly visible in this figure and consistent with the expected wavelength at 500 Hz (approx. 10 mm) for plastisol phantom [\[33\]](#). The subtraction of two linear and periodic phase distributions with a  $180^\circ$  phase shift is a square distribution consistent with the phase distribution in [Fig. 11](#).

As a comparison, a conventional MRE experiment was also performed, with a gradient echo sequence at the same excitation frequency (500 Hz), and with the following parameters:  $\text{TE} = 14 \text{ ms}$  (minimum echo-time achievable),  $\text{TR} = 1500 \text{ ms}$ ,  $\text{FOV} = 4 \times 4 \text{ cm}^2$ ,  $64 \times 64$  matrix, 2 accumulations, slice thickness = 500  $\mu\text{m}$ , and 4 encoding phase steps.

##### 6.6.2. Reconstruction of elastic properties

Shear storage modulus ( $G$ ) has been calculated from phase images obtained with conventional MRE and OC MRE, with a well-established Helmholtz inversion algorithm and reconstruction pipeline detailed in the reference [\[33\]](#). In short, the resulting four image offsets, corresponding to four snapshots of the wave propagation over one cycle, were temporally Fourier transformed, and the first harmonic (corresponding to the excitation frequency) was extracted. Next a band-pass Butterworth filter was applied to remove noise. Finally, storage modulus, corresponding to the elasticity of the phantom, was determined by applying a 2D Helmholtz inversion algorithm.

[Fig. 12](#) presents the real part of the temporal filtered Fourier transform of phase images obtained from conventional MRE and from OC MRE. Both images display a similar wavelength. Note that the first harmonic of the Fourier transform of a square wave ([Fig. 11](#)) is a sinusoid at the same frequency, and it is therefore consistent with [Fig. 12](#).

A Region of Interest (ROI), excluding the edges of the phantom, was defined on the obtained elastograms. The mean storage modulus for conventional MRE was  $G' = 25.9 \pm 1.72 \text{ kPa}$ , and for OC

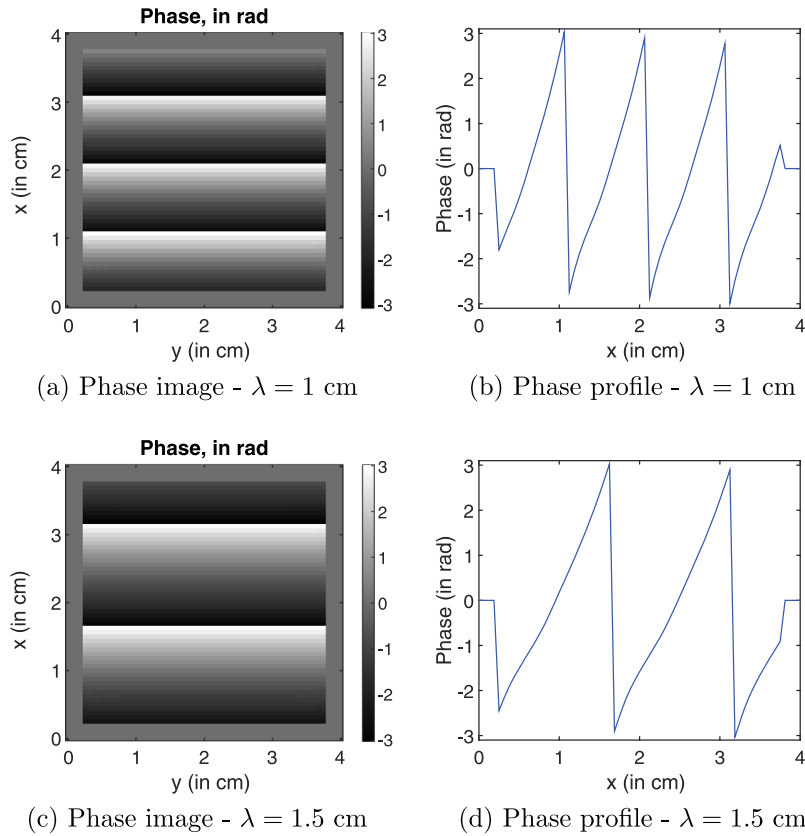


**Fig. 10.** Phase images (in radians) obtained from the optimal RF pulse associated to the elastography problem, with the ODIN MRI simulation for two different wavelengths ( $\lambda = 1 \text{ cm}$  and  $\lambda = 1.5 \text{ cm}$ ), and their corresponding profiles.

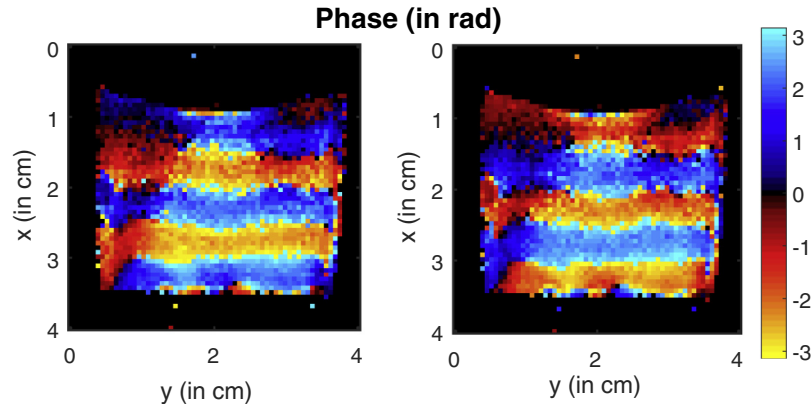


**Fig. 11.** Phase images (in radians) obtained from the subtraction of the two MRE experiments with a 180° phase shift, at two different time steps of wave propagation (90° phase shift between these two images).

MRE  $G' = 24.2 \pm 3.35 \text{ kPa}$ . Despite a slightly higher standard deviation, the average storage modulus obtained for OC MRE is comparable to the one of conventional MRE. This shows that an MRE experiment performed with OC-designed RF pulses can give elasticity values comparable to the classical approach.

## 7. Discussion

Our goal in this paper was to explore the use of RF pulses, designed with optimal control theory, to actively control the MR phase signal.

First, resulting phase images in Sections 4 and 5 present a very good agreement with the desired phase patterns, in both simula-

tions and experiments on phantom. These initial results validate the ability of optimal RF pulses to control the magnetization phase, based on the spins oscillation frequency. Note that in this study, the phase pattern was arbitrarily created in the readout direction. The results can be extended to any other dimension with the same RF pulses.

These pulses were calculated for specific  $T_1$  and  $T_2$  values, as they have to be specified in the Bloch equations. However, pulses A and B can be used with tissues presenting different  $T_1$  and  $T_2$  values or with heterogeneous tissues: numerical simulations were performed (and not shown here) and obtained phase profiles were not affected by a change in the relaxation times.

Computation times required for the design of the RF pulses A and B depend on the frequency range offset. Running the algorithm

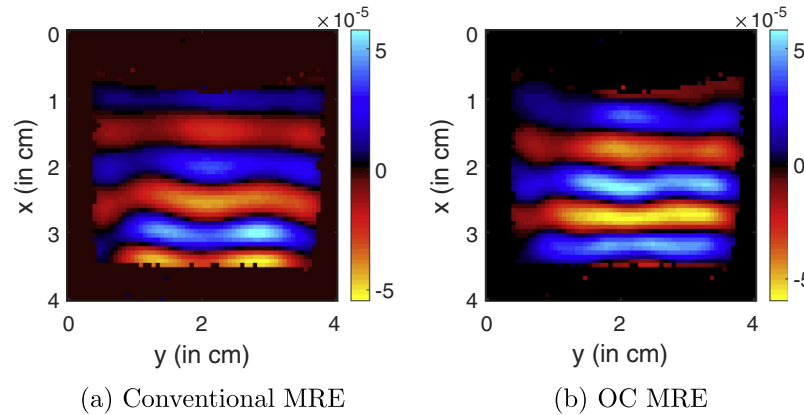


**Fig. 12.** Real part of the temporal filtered Fourier transform of phase images obtained from conventional MRE and OC MRE.

on a  $4 \times 2.7$  GHz machine using Matlab (The MathWorks, Inc., Natick, MA, USA, R2014b) takes less than fifteen minutes for a frequency range of 10 kHz, with a frequency discretization of 50 Hz (200 intervals considered in the frequency range offset), as it has been chosen in this study.

The current implementation of the optimization algorithm requires a unique magnetization state as a boundary condition, which was chosen here as the thermal equilibrium. Thus, the acquisition strategy requires long TRs, as we have to wait for full longitudinal relaxation after each excitation, before performing the next RF pulse. However, a turbo spin-echo sequence could be used to accelerate the acquisition.

After these initial experiments, the use of optimal RF pulses in a more practical framework was investigated. MRE was chosen as a proof-of-concept, and results presented in Section 6 show, for the first time, the possibility to acquire MRE phase images without an oscillating gradient but with a combination of a RF pulse and a constant gradient. This shows the ability of optimal RF pulses to accurately control the phase in the presence of a dynamic evolution of the static field.

A first advantage of using optimal RF pulses here is the very short echo-time achievable. In standard MRE sequences, motion-encoding gradients typically last between 5 and 10 ms and lengthen therefore the echo-time. During this time, magnetization relaxation occurs and this echo-time increase can be critical for some tissues with very short  $T_2$ , as in the healthy mouse liver where  $T_2$  value is equal to about 20 ms at 7 T [35], or at low frequency (where duration of the MEG is longer). OC-designed RF pulses take into account  $T_2$  relaxation during optimization process and thus maximize signal at the end of the OC pulse.

Using OC RF pulses also relaxes the constraint on having a periodic gradient, and thus avoids fast gradient switching which is a hardware limitation. Some MRE applications require very high frequencies, in the kilohertz range [36], which are not achievable in standard MRI systems. The use of OC pulse can be a solution to image shear waves in these frequency ranges.

Slice selectivity is controlled in this MRE case by the combination of a frequency offset range (on which the pulse has been optimized) and a gradient in the slice direction, that is also the motion direction. However, it is hard to predict the behavior of the spins that lie outside the control range. This could explain the noise observed in the MRE phase images in Fig. 11. Results presented here on MRE are preliminary but encouraging, as wave propagation is clearly encoded in the phase images and reconstructed storage modulus  $G'$  consistent. Future improvements will imply a better understanding of spin behavior outside the control range, and the investigation of new cost function definitions.

## 8. Conclusion

This work validates the use of optimal control RF pulses to accurately and actively control the magnetization phase in MRI. As a proof-of-concept, RF pulses were computed to create non-trivial phase patterns. Both simulations and experiments on phantom present good match with the desired patterns. Optimal RF pulses were also designed in the context of MR elastography, to show their interest in a more practical framework. Preliminary results demonstrate, for the first time, that optimal RF pulses can be used to encode the dynamic wave propagation without the use of oscillating gradients.

RF-based phase encoding would present several advantages over standard techniques based on gradient switching (shorter TE, reduction of eddy currents, ability to overcome limitations due to gradient switching rates). This work can open new research fields on MRI phase-based sequences, with the use of RF pulses that directly encode physical information in the MR phase image.

#### Acknowledgment

This work is supported by the ANR-DFG research program Explosys (Grant No. ANR-14-CE35-0013-01; GL203/9-1) and from the Technische Universität München Institute for Advanced Study, funded by the German Excellence Initiative and the EU Seventh Framework Programme under Grant No. 291763. This work was performed within the framework of the LABEX PRIMES (ANR-11-LABX-0063/ANR-11-IDEX-0007).

## References

- [1] N.J. Pelc, R.J. Herfkens, A. Shimakawa, D.R. Enzmann, Phase contrast cine magnetic resonance imaging, Magn. Reson. Q. 7 (4) (1991) 229–254.
  - [2] E.M. Haacke, Y. Xu, Y.-C.N. Cheng, J.R. Reichenbach, Susceptibility weighted imaging (SWI), Magn. Reson. Med. 52 (3) (2004) 612–618, <http://dx.doi.org/10.1002/mrm.20198>.
  - [3] R. Muthupillai, D.J. Lomas, P.J. Rossman, J.F. Greenleaf, A. Manduca, R.L. Ehman, Magnetic resonance elastography by direct visualization of propagating acoustic strain waves, Science. 269 (September) (1995) 1854–1857, <http://dx.doi.org/10.1126/science.7569924>.
  - [4] J. De Poorter, C. De Wagter, Y. De Deen, C. Thomsen, F. Stahlberg, E. Achten, Noninvasive MRI thermometry with the proton resonance frequency (PRF) method: in vivo results in human muscle, Magn. Reson. Med. 33 (1) (1995) 74–81, <http://dx.doi.org/10.1002/mrm.1910303111>.
  - [5] P.J. Basser, D.K. Jones, Diffusion-tensor MRI: theory, experimental design and data analysis - a technical review, NMR Biomed. 15 (7–8) (2002) 456–467, <http://dx.doi.org/10.1002/nbm.783>.
  - [6] J. Pauly, P. Le Roux, D. Nishimura, A. Macovski, Parameter relations for the Shinnar-Le Roux selective excitation pulse design algorithm, IEEE Trans. Med. Imaging. 10 (1) (1991) 53–65, <http://dx.doi.org/10.1109/42.75611>.

- [7] P. Le Roux, R. Gilles, G. McKinnon, P. Carlier, Optimized outer volume suppression for single-shot fast spin-echo cardiac imaging, *J. Magn. Reson. Imag.* 8 (5) (1998) 1022–1032, <http://dx.doi.org/10.1002/jmri.1880080505>.
- [8] J.W. Carlson, Exact solutions for selective excitation pulses. II. Excitations pulses with phase control, *J. Magn. Res.* 97 (1) (1992) 65–78, [http://dx.doi.org/10.1016/0022-2364\(92\)90237-2](http://dx.doi.org/10.1016/0022-2364(92)90237-2).
- [9] J.W. Carlson, Nonlinear phase adjustment of selective excitation pulses, *J. Mag. Res.* 147 (2) (2000) 210–216, <http://dx.doi.org/10.1006/jmre.2000.2201>.
- [10] S.J. Glaser, U. Boscain, T. Calarco, C.P. Koch, W. Köckenberger, R. Kosloff, I. Kuprov, B. Luy, S. Schirmer, T. Schulte-Herbrüggen, D. Sugny, F.K. Wilhelm, Training Schrödinger's cat: quantum optimal control – strategic report on current status, visions and goals for research in Europe, *Eur. Phys. J. D* 69 (December) (2015) 279, <http://dx.doi.org/10.1140/epjd/e2015-60464-1>.
- [11] S. Conolly, D. Nishimura, A. Macovski, Optimal control solutions to the magnetic resonance selective excitation problem, *IEEE Trans. Med. Im.* 5 (2) (1986) 106–115, <http://dx.doi.org/10.1109/TMI.1986.4307754>.
- [12] T.E. Skinner, T.O. Reiss, B. Luy, N. Khaneja, S.J. Glaser, Application of optimal control theory to the design of broadband excitation pulses for high-resolution NMR, *J. Magn. Res.* 163 (1) (2003) 8–15, [http://dx.doi.org/10.1016/S1090-7807\(03\)00153-8](http://dx.doi.org/10.1016/S1090-7807(03)00153-8).
- [13] T.E. Skinner, N.I. Gershenzon, M. Nimbalkar, W. Bermel, B. Luy, S.J. Glaser, New strategies for designing robust universal rotation pulses: application to broadband refocusing at low power, *J. Magn. Res.* 216 (March) (2012) 78–87, <http://dx.doi.org/10.1016/j.jmr.2012.01.005>.
- [14] C.S. Aigner, C. Clason, A. Rund, R. Stollberger, Efficient high resolution RF pulse design applied to simultaneous multi-slice excitation, *J. Magn. Res.* 263 (February) (2016) 33–44, <http://dx.doi.org/10.1016/j.jmr.2015.11.013>.
- [15] B. Bonnard, O. Cots, S. Glaser, M. Lapert, D. Sugny, Y. Zhang, Geometric optimal control of the contrast imaging problem in nuclear magnetic resonance, *IEEE Trans. Autom. Control* 57 (8) (2012) 1957–1969, <http://dx.doi.org/10.1109/TAC.2012.2195859>.
- [16] M. Lapert, Y. Zhang, M. Janich, S. Glaser, D. Sugny, Exploring the physical limits of saturation contrast in magnetic resonance imaging, *Sci. Rep.* 2 (2012) 589, <http://dx.doi.org/10.1038/srep00589>.
- [17] B. Bonnard, M. Claeys, O. Cots, P. Martinon, Geometric and numerical methods in the contrast imaging problem in nuclear magnetic resonance, *Acta Appl. Math.* 135 (1) (2014) 5–45, <http://dx.doi.org/10.1007/s10440-014-9947-3>.
- [18] E. Van Reeth, H. Ratiney, M. Tesch, S.J. Glaser, D. Sugny, Optimizing MRI contrast with B1 pulses using optimal control theory, *IEEE 13th International Symposium on Biomedical Imaging*, Prague (2016), <http://dx.doi.org/10.1109/ISBI.2016.7493271>.
- [19] D. Xu, K.F. King, Y. Zhu, G.C. McKinnon, Z.-P. Liang, Designing multichannel, multidimensional, arbitrary flip angle RF pulses using an optimal control approach, *Magn. Res. Med.* 59 (3) (2008) 547–560, <http://dx.doi.org/10.1002/mrm.21485>.
- [20] A. Massire, M.A. Cloos, A. Vignaud, D.L. Bihan, A. Amadon, N. Boulant, Design of non-selective refocusing pulses with phase-free rotation axis by gradient ascent pulse engineering algorithm in parallel transmission at 7 T, *J. Magn. Res.* 230 (May) (2013) 76–83, <http://dx.doi.org/10.1016/j.jmr.2013.01.005>.
- [21] A. Sbrizzi, H. Hoogduin, J.V. Hajnal, C.A. van den Berg, P.R. Luijten, S.J. Malik, Optimal control design of turbo spin-echo sequences with applications to parallel-transmit systems, *Magn. Res. Med.* 77 (1) (2017) 361–373, <http://dx.doi.org/10.1002/mrm.26084>.
- [22] K. Kobzar, B. Luy, N. Khaneja, S.J. Glaser, Pattern pulses: design of arbitrary excitation profiles as a function of pulse amplitude and offset, *J. Magn. Reson.* 173 (2) (2005) 229–235, <http://dx.doi.org/10.1016/j.jmr.2004.12.005>.
- [23] N.I. Gershenzon, T.E. Skinner, B. Brutscher, N. Khaneja, M. Nimbalkar, B. Luy, S. J. Glaser, Linear phase slope in pulse design: application to coherence transfer, *J. Magn. Reson.* 192 (2) (2008) 235–243, <http://dx.doi.org/10.1016/j.jmr.2008.02.021>.
- [24] J. Assländer, S.J. Glaser, J. Hennig, Spin echoes in the regime of weak dephasing, *Magn. Res. Med.* 75 (1) (2016) 150–160, <http://dx.doi.org/10.1002/mrm.25579>.
- [25] T.H. Jochimsen, M. Von Mengeshausen, ODIN-object-oriented development interface for NMR, *J. Magn. Res.* 170 (1) (2004) 67–78, <http://dx.doi.org/10.1016/j.jmr.2004.05.021>.
- [26] N. Baril, C.J. Lewa, J.D. de Certaines, P. Canioni, J.-M. Franconi, E. Thiaudiére, MR detection of mechanical vibrations using a radiofrequency field gradient, *J. Magn. Res.* 154 (4) (2002) 22–27, <http://dx.doi.org/10.1006/jmre.2001.2451>.
- [27] L.S. Pontryagin, B. Boltyanskii, R. Gamkrelidze, E. Mishchenko, *The Mathematical Theory of Optimal Processes*, Wiley Interscience, New York, 1962.
- [28] N. Khaneja, T. Reiss, C. Kehlet, T. Schulte-Herbrüggen, S.J. Glaser, Optimal control of coupled spin dynamics: design of NMR pulse sequences by gradient ascent algorithms, *J. Magn. Res.* 172 (2) (2005) 296–305, <http://dx.doi.org/10.1016/j.jmr.2004.11.004>.
- [29] M. Lapert, On GRAPE Implementation, Private Note, April 2016.
- [30] W. Squire, G. Trapp, Using complex variables to estimate derivatives of real functions, *SIAM Rev.* 40 (1) (1998) 110–112, <http://dx.doi.org/10.1137/S003614459631241X>.
- [31] P. de Fouquieres, S. Schirmer, S. Glaser, I. Kuprov, Second order gradient ascent pulse engineering, *J. Magn. Res.* 212 (2) (2011) 412–417, <http://dx.doi.org/10.1016/j.jmr.2011.07.023>.
- [32] P.M. Lefebvre, E. Van Reeth, E. Brusseau, D. Grenier, K. Tse Ve Koon, Magnetic resonance elastography simulation with an object oriented development interface for NMR, in: 33rd Annual ESMRMB Congress, Vienna, Austria, 2016, doi:<http://dx.doi.org/10.1007/s10334-016-0568-x>.
- [33] P.M. Lefebvre, K. Tse Ve Koon, E. Brusseau, S. Nicolle, J.F. Palierne, S.A. Lambert, D. Grenier, Comparison of viscoelastic property characterization of plastisol phantoms with magnetic resonance elastography and high-frequency rheometry, *IEEE 38th Conference of the Engineering in Medicine and Biology Society*, Orlando (2016) 1216–1219, <http://dx.doi.org/10.1109/EMBC.2016.7590924>.
- [34] Y.K. Mariappan, K.J. Glaser, R.L. Ehman, Magnetic resonance elastography: a review, *Clin. Anat.* 23 (5) (2010) 497–511, <http://dx.doi.org/10.1002/ca.21006>.
- [35] A.M. Chow, D.S. Gao, S.J. Fan, Z. Qiao, F.Y. Lee, J. Yang, K. Man, E.X. Wu, Measurement of liver T1 and T2 relaxation times in an experimental mouse model of liver fibrosis, *J. Magn. Reson. Imag.* 36 (1) (2012) 152–158, <http://dx.doi.org/10.1002/jmri.23606>.
- [36] O. Lopez, K.K. Amrami, A. Manduca, P.J. Rossman, R.L. Ehman, Developments in dynamic MR elastography for in vitro biomechanical assessment of hyaline cartilage under high-frequency cyclical shear, *J. Magn. Reson. Imag.* 25 (2) (2007) 310–320, <http://dx.doi.org/10.1002/jmri.20857>.